Objective vortex detection in an astrophysical dynamo

Monthly Notices of the ROYAL ASTRONOMICAL SOCIETY

MNRAS **466,** L108–L112 (2017) doi:10.1093/mnrasl/slw248
Advance Access publication 2016 December 10

Objective vortex detection in an astrophysical dynamo

E. L. Rempel,[1,2]★ A. C.-L. Chian,[1,2,3] F. J. Beron-Vera,[4] S. Szanyi[5] and G. Haller[5]

[1]*Institute of Aeronautical Technology (ITA), World Institute for Space Environment Research (WISER), São José dos Campos, SP 12228–900, Brazil*
[2]*National Institute for Space Research (INPE), PO Box 515, São José dos Campos, SP 12227-010, Brazil*
[3]*School of Mathematical Sciences, University of Adelaide, Adelaide, SA 5005, Australia*
[4]*Rosenstiel School of Marine & Atmospheric Science, University of Miami, 4600 Rickenbacker Causeway, Miami, FL 33149, USA*
[5]*Institute for Mechanical Systems, Department of Mechanical and Process Engineering, ETH, Leonhardstrasse 21, LEE M25, CH-8092 Zürich, Switzerland*

Accepted 2016 December 6. Received 2016 December 6; in original form 2016 October 31

ABSTRACT

A novel technique for detecting Lagrangian vortices is applied to a helical magnetohydrodynamic dynamo simulation. The vortices are given by tubular level surfaces of the Lagrangian averaged vorticity deviation, the trajectory integral of the normed difference of the vorticity from its spatial mean. This simple method is objective, i.e. invariant under time-dependent rotations and translations of the coordinate frame. We also adapt the technique to use it on magnetic fields and propose the method of integrated averaged current deviation to determine precisely the boundary of magnetic vortices. The relevance of the results for the study of vortices in solar plasmas is discussed.

Key words: chaos – dynamo – MHD.

1 INTRODUCTION

The analysis of fluid or plasma flows can be a daunting task, given the number of temporal and spatial scales involved, especially in turbulent or strongly chaotic systems. In order to achieve some complexity reduction, one can try to detect certain coherent structures that act as protagonists in the dynamics, in the sense that they provide the most attracting or repelling regions of the flow, acting as transport barriers and dividing the phase space in regions with qualitatively different behaviour. Coherent structures have been roughly defined as 'persistent localized features in time-varying fields' (Peacock, Froyland & Haller 2015). In velocity fields, such structures are usually defined in terms of the vorticity of the flow or some related quantity, being identified as vortices or eddies. There is no standard way to define a vortex, with definitions adopting a Eulerian or a Lagrangian approach. In Eulerian definitions, the vortices are extracted from the velocity field at a given time (see e.g. the Q-criterion; Rempel et al. 2013), whereas in the Lagrangian approach the evolution of a set of fluid particles in space and time is taken into account. This has led to the theory of Lagrangian coherent structures (LCSs) in the past two decades (Haller 2015; Peacock et al. 2015). There are several different kinds of LCSs, depending on whether one wants to describe hyperbolic, parabolic or elliptic regions of the flow. Recently, a new kind of LCS has been identified based on the integrated deviation of the vorticity from its spatial mean along fluid particles. These rotational LCSs (Haller et al. 2016) are formed by material tubes of particles that exhibit the same average rotation, identified from a new dynamic version of the classic polar decomposition (Haller 2016).

Magnetic coherent structures are often associated with magnetic flux tubes/ropes. One of the common features of flux ropes is that the magnetic field lines at one location along the rope must wind around and not diverge away from each other over a sufficiently long distance to look like a piece of an ordinary rope (Lukin 2014). Thus, magnetic flux tubes are a bundle of magnetic field lines in a cylindrical region inside which the axial magnetic field is much larger than the magnetic field outside, whereas a magnetic flux rope is a twisted flux tube, with helical field lines. Flux tubes and ropes need not be straight, and their cross-sections can be neither circular, nor uniform along their lengths. The definition above leaves out a precise description of what is the boundary of a flux rope, since one needs to arbitrarily specify where magnetic field lines are considered inside or outside the rope, based on a pre-defined magnetic field threshold or rope width. An accurate detection of the boundary of coherent structures is fundamental for the study of astrophysical turbulence, e.g. the determination of the front and rear boundary layers of magnetic flux ropes in the solar wind is essential for locating the preferential sites for genesis of interplanetary intermittent turbulence (Chian et al. 2016). Similarly, knowledge of the magnetic topology of emerging flux ropes in the solar atmosphere is important to understand the reconnection of the rope with the coronal field, with implications for solar eruptions (MacTaggart and Haynes 2014).

In this Letter, we employ rotational LCSs to find kinematic vortices in the problem of a magnetohydrodynamic (MHD) dynamo. We also adapt the definition to use it on magnetic fields and propose a method to detect with precision the boundary of magnetic vortices.

★ E-mail: rempel@ita.br

2 EULERIAN AND LAGRANGIAN VORTICES

Consider a spatial flow domain U, with a velocity field $\boldsymbol{u}$, its vorticity $\boldsymbol{\omega} = \nabla \times \boldsymbol{u}$ and let $\bar{\boldsymbol{\omega}}$ be the instantaneous spatial mean of $\boldsymbol{\omega}$. Fluid particle trajectories (*pathlines*) are solutions of the system $\dot{\boldsymbol{x}} = \boldsymbol{u}(\boldsymbol{x}, t)$, with the initial condition $\boldsymbol{x}(t_0) = \boldsymbol{x}_0$. Define the instantaneous vorticity deviation (IVD) of a particle as $\mathrm{IVD}(\boldsymbol{x}, t) := |\boldsymbol{\omega}(\boldsymbol{x}, t) - \bar{\boldsymbol{\omega}}(t)|$. The Lagrangian averaged vorticity deviation (LAVD) is defined by Haller et al. (2016) as the integrated IVD along a fluid particle trajectory, i.e.

$$\mathrm{LAVD}_{t_0}^{t_0+\tau}(\boldsymbol{x}_0) := \int_{t_0}^{t_0+\tau} |\boldsymbol{\omega}(\boldsymbol{x}(s), s) - \bar{\boldsymbol{\omega}}(s)| \mathrm{d}s. \quad (1)$$

From that, for a given finite time interval $[t_0, t_0 + \tau]$, a rotationally coherent Lagrangian vortex is defined as an evolving material domain $\mathcal{V}_\mathrm{L}(t)$ such that $\mathcal{V}_\mathrm{L}(t_0)$ is filled with a nested family of convex tubular level surfaces of $\mathrm{LAVD}_{t_0}^{t_0+\tau}(\boldsymbol{x}_0)$ with outward-decreasing LAVD values; the boundary of $\mathcal{V}_\mathrm{L}(t)$ is the outermost convex tubular level surface of $\mathrm{LAVD}_{t_0}^{t_0+\tau}(\boldsymbol{x}_0)$ in $\mathcal{V}_\mathrm{L}(t_0)$. Each of the tubular level surfaces belonging to $\mathcal{V}_\mathrm{L}(t)$ is called a *rotational LCS*. Similarly, a rotationally coherent Eulerian vortex is a set $\mathcal{V}_\mathrm{E}(t)$ filled with a nested family of convex tubular level sets of $\mathrm{IVD}(\boldsymbol{x}, t)$ with outwards non-increasing IVD values; the boundary of $\mathcal{V}_\mathrm{E}(t)$ is the outermost convex tubular level surface of $\mathrm{IVD}(\boldsymbol{x}, t)$ in $\mathcal{V}_\mathrm{E}(t)$. All these definitions follow from considerations based on the dynamic polar decomposition of the deformation gradient (Haller 2016).

The intersection of Lagrangian (Eulerian) vortices with a plane in the domain U can be readily extracted from velocity fields by computing the LAVD (IVD) field from a grid of initial particles at the plane, detecting the initial positions of vortex centres as local maxima of LAVD (IVD), then seeking vortex boundaries as outermost *convex* closed contours of LAVD (IVD) that encircle vortex centres. In practical implementations, the level curves will be strictly speaking non-convex polygons due to their jaggedness caused by finite data resolution. Thus, we accept a small convexity deficiency, ε, defined as the ratio of the area difference between the curve and its convex hull to the area enclosed by the curve. The choice of ε does not depend on the original flow resolution, but on the interpolated LAVD field. A generally good choice for ε for an interpolated field with 512^3 points, as used here, is between 10^{-3} and 10^{-5}, which tends to eliminate non-convexity due to numerical discretization, yet avoids classifying numerical approximations of non-convex structures as convex. We illustrate the technique showing vortex detection for the stationary ABC (Arnold–Beltrami–Childress) flow, $\boldsymbol{u}_\mathrm{ABC} = A_\mathrm{f}/\sqrt{3}\,[(\sin k_\mathrm{f} z + \cos k_\mathrm{f} y)\hat{\boldsymbol{x}}\ , (\sin k_\mathrm{f} x + \cos k_\mathrm{f} z)\hat{\boldsymbol{y}},\ (\sin k_\mathrm{f} y + \cos k_\mathrm{f} x)\hat{\boldsymbol{z}}]$, where A_f is the amplitude and k_f the wavenumber of the forcing function. Fig. 1(a) shows a Lagrangian velocity vortex in the stationary ABC-flow for $A_\mathrm{f} = \sqrt{3}$ and $k_\mathrm{f} = 1$; the vortex boundary (white curve) was obtained from the LAVD field at the plane $z = 0$ using a convexity deficiency of the order of 10^{-5}. Also plotted are the forward-time (green) and backward-time (red) maximum finite-time Lyapunov exponent (FTLE) fields, that have frequently been associated with repelling and attracting barriers to particle transport in flows (see however, Haller 2015 for caveats). Fig. 1(b) depicts the pathlines of initial conditions on the blue curve, which is the same as the white curve in the upper panel. Note that these particles spiral around a tubular region of the flow. If a slightly wider curve is used for the initial conditions, the particle trajectories lose their global coherence and spread throughout the box, as in Fig. 1(c). This shows the importance of accurately finding the vortex boundary. A similar analysis of LAVD-based vortices in the ABC flow appears in Haller et al. (2016).

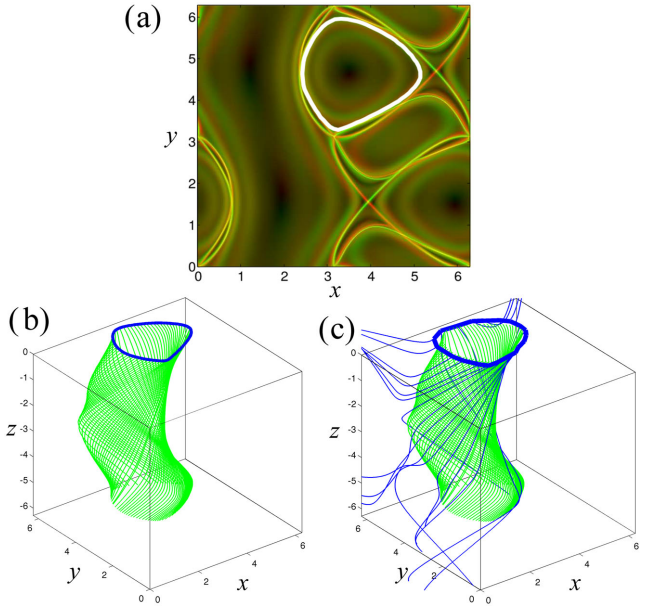

Figure 1. Lagrangian vortex in a stationary ABC-flow. (a) The forward- (green) and backward- (red) time FTLE for initial conditions on a plane at $z = 0$. The white line represents the coherent Lagrangian vortex obtained from the LAVD field of the ABC-flow; (b) 3D Lagrangian coherent vortex revealed by the pathlines of initial conditions on the blue curve, which is the same as the white curve in the upper panel; (c) the pathlines from a curve slightly wider than the one in (b).

3 RESULTS

The dynamo model adopted consists of the compressible MHD equations for an isothermal fluid, as described by Rempel, Proctor & Chian (2009). The computational domain is a box with sides $L = 2\pi$ and periodic boundary conditions, so the smallest wavenumber is $k_1 = 1$. The sound speed is $c_\mathrm{s} = 1$, so the time unit is $(c_\mathrm{s} k_1)^{-1}$ and the unit of viscosity ν and magnetic diffusivity η is c_s/k_1. Space is measured in units of k_1^{-1}, the velocity field $\boldsymbol{u}$ in units of c_s, the density ρ in units of the mean density ρ_0, the magnetic field $\boldsymbol{B}$ in units of $(\mu_0 \rho_0)^{1/2} c_\mathrm{s}$, where μ_0 is the constant magnetic permeability. We add to the momentum equation an external forcing given by the ABC function, $\boldsymbol{f}(\boldsymbol{x}) = \boldsymbol{u}_\mathrm{ABC}$, with $k_\mathrm{f} = 5$ as the forcing scale, and an amplitude regulated by $A_\mathrm{f} = 0.1$. The MHD equations are solved with the PENCIL CODE,[1] which employs an explicit sixth-order finite differences scheme in space and a variable-step third-order Runge–Kutta scheme for time integration. Following Rempel, Proctor & Chian (2009) and Rempel, Chian & Brandenburg (2011), we set $\nu = 0.005$, $\eta = 0.01$ and the numerical resolution of 64^3 mesh points is chosen.

After an initial exponential growth of the magnetic energy in the so-called *kinematic dynamo* phase, the field growth is nonlinearly saturated as shown in Fig. 2(a). The kinetic (dashed line) and magnetic (solid line) energy spectra at $t = 700$ are shown in Fig. 2(b). The B_z component in the initial kinematic phase is shown in Fig. 2(c), whereas B_z in the saturated phase is shown in Fig. 2(d), where a large-scale field pattern is noticed.

First, we obtain objective Eulerian and Lagrangian vortices from the velocity field of the dynamo simulations and check the behaviour of fluid particles in those vortices. In order to solve the equation $\dot{\boldsymbol{x}} = \boldsymbol{u}$ to obtain the particles' pathlines, we need a velocity field that

[1] http://pencil-code.googlecode.com/

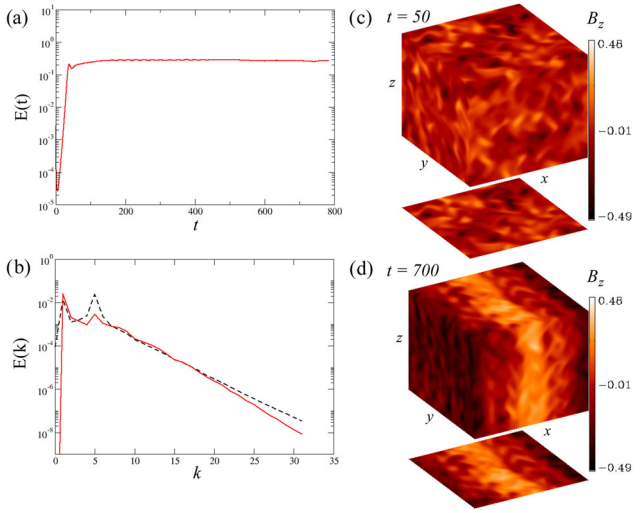

Figure 2. Non-linear dynamo simulation. (a) The magnetic energy time series, showing the initial exponential growth of the seed field, followed by its non-linear saturation. (b) The magnetic (red solid line) and kinetic (black dashed line) power spectra at $t = 750$. Note that the main peak for the kinetic spectrum is at the energy-injection wavenumber $k = 5$, whereas for the magnetic field the main peak is at $k = 1$. (c) The B_z component of the magnetic field for $t = 50$ and (d) for $t = 700$, showing the appearance of a large-scale mean-field amidst the small-scale fluctuations.

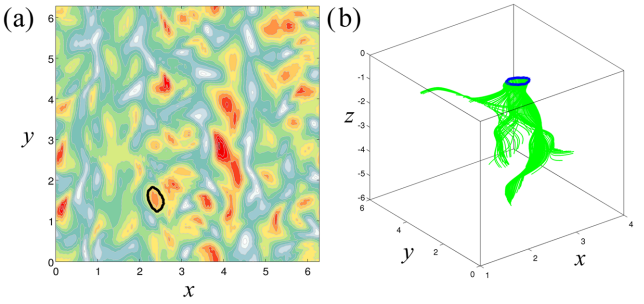

Figure 3. Objective Eulerian vortex detection for the unsteady dynamo simulation. (a) The contour plot of the IVD for the velocity field at $z = 0$; the black curve is the boundary of a Eulerian vortex. (b) The pathlines of a set of particles initially on the Eulerian vortex boundary shown in (a).

is continuous in space and time. For that matter, we save the velocity field every 0.2 time units from $t_0 - \tau$ to $t_0 + \tau$, using $t_0 = 700$ and $\tau = 10$, and adopt cubic splines to interpolate the three-dimensional fields in time and space. The pathlines are obtained from the interpolated fields using a fourth-order Runge–Kutta integrator with a time step $\Delta t = 0.002$.

We compute objective Eulerian vortices in the velocity field by using the IVD at $t = 700$. Fig. 3(a) shows the contour plot of IVD for $\boldsymbol{u}$ at $z = 0$. The black curve is the boundary of a vortex found with the method described in Section 2. Fig. 3(b) shows the pathlines of a set of fluid particles initially placed on the vortex boundary, revealing that the Eulerian vortex detection using instantaneous vorticity is not useful to determine coherent structures in this case, since it is based on a single plane of the domain and it does not take into account the time evolution of the velocity field. This was to be expected, since the purpose of IVD is to give an objective assessment of short-term coherence, not to forecast long-term Lagrangian coherence.

Next, we solve equation (1) for $t_0 = 700$, $\tau = 10$ and a grid of points $\boldsymbol{x}_0$ on $z = 0$. The contour plot of this LAVD field is shown

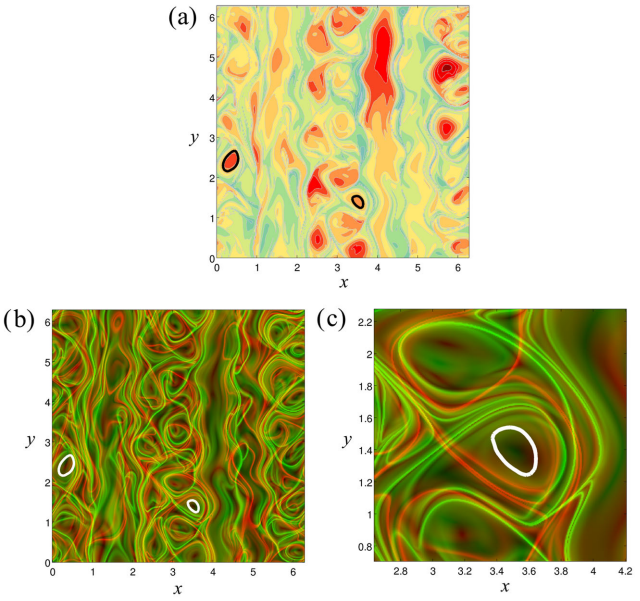

Figure 4. Objective Lagrangian vortices in the unsteady dynamo simulation. (a) The contour plot of the LAVD of the velocity field at $z = 0$. The black curves represent two Lagrangian vortex boundaries; (b) superposition of the Lagrangian vortices on the forward-time (green) and backward-time (red) FTLE fields; (c) enlargement of a region near the rightward vortex in (b), showing the Lagrangian vortex surrounded by lines of local maxima of the FTLE fields.

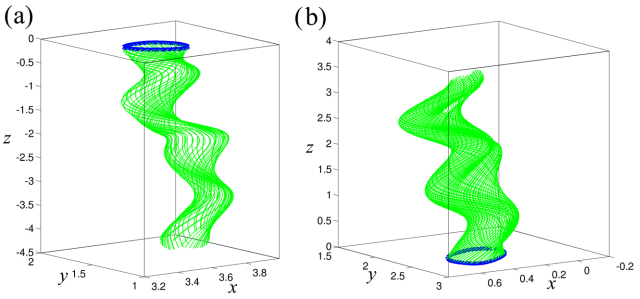

Figure 5. 3D Lagrangian velocity vortices in the unsteady dynamo simulation. (a) The pathlines of initial conditions on the rightward vortex in Fig. 4; (b) the pathlines of initial conditions on the leftward vortex in Fig. 4.

in Fig. 4(a), together with two selected vortices extracted with a convexity deficiency of the order of 10^{-3}. Fig. 4(b) shows the same vortices superposed on the forward-time (green) and backward-time (red) FTLE. Fig. 4(c) is an enlargement of a box in Fig. 4(b). By integrating the fluid particles from the vortex boundaries found in Fig. 4, one can see that the material coherence of the vortex is kept through space and time, as depicted in Fig. 5.

In order to extract objective magnetic vortices, we propose an adaptation of the LAVD operator for the magnetic field. Consider a parametrization of a magnetic field line at time t_0 given by $\boldsymbol{x}(s)$, where s is a parameter related to the distance l along the field line by $\mathrm{d}l = |\boldsymbol{B}|\mathrm{d}s$. Then, the field-line equation at t_0 is given by (Sonsrettee et al. 2015)

$$\frac{\mathrm{d}\boldsymbol{x}}{\mathrm{d}s} = \boldsymbol{B}(\boldsymbol{x}(s), t_0), \quad \boldsymbol{x}(s_0) = \boldsymbol{x}_0. \tag{2}$$

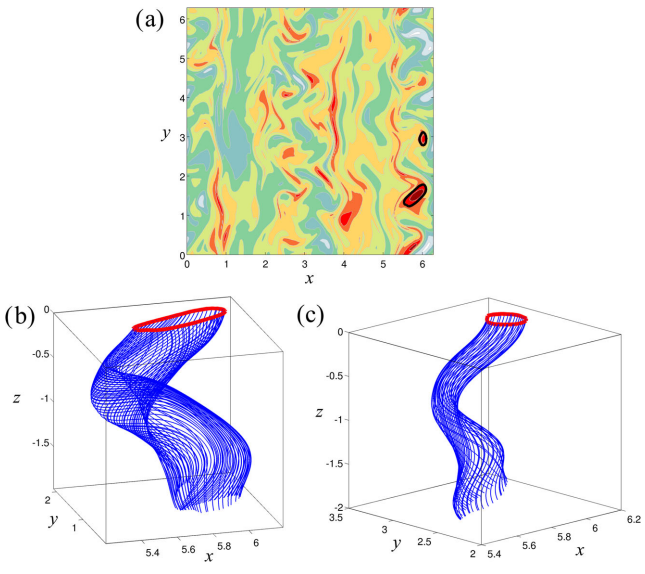

Figure 6. Objective magnetic vortices in the unsteady dynamo simulation. (a) The contour plot of the IACD of the magnetic field at $z = 0$ and $t_0 = 700$. The black curves represent two Lagrangian magnetic vortex boundaries; (b) magnetic field lines from initial conditions on the lower vortex boundary shown in (a); (c) magnetic field lines from initial conditions on the upper vortex boundary in (a).

The integrated averaged current deviation (IACD) field can be computed for $\boldsymbol{B}$ in essentially the same way as LAVD is for $\boldsymbol{u}$, by using $\boldsymbol{J} = \nabla \times \boldsymbol{B}/\mu_0$ in place of $\boldsymbol{\omega} = \nabla \times \boldsymbol{u}$:

$$\mathrm{IACD}_{s_0}^{s_0+\xi}(\boldsymbol{x}_0) := \int_{s_0}^{s_0+\xi} |\boldsymbol{J}(\boldsymbol{x}(s), t_0) - \bar{\boldsymbol{J}}(t_0)| \mathrm{d}s, \tag{3}$$

where $\boldsymbol{x}(s)$ is a solution of equation (2) and $\bar{\boldsymbol{J}}(t_0)$ is the mean current density of the box at t_0. Note that, different from LAVD, here the calculations are done for a fixed time t_0, since the field-line equations, equation (2), are defined for a fixed time. For a given parameter interval $[s_0, s_0 + \xi]$, we define a magnetic vortex as a domain $\mathcal{V}_\mathrm{L}(t_0)$ such that $\mathcal{V}_\mathrm{L}(t_0)$ is filled with a nested family of convex tubular level surfaces of $\mathrm{IACD}_{s_0}^{s_0+\xi}(\boldsymbol{x}_0)$ with outward-decreasing IACD values; the boundary of $\mathcal{V}_\mathrm{L}(t_0)$ is the outermost convex tubular level surface of $\mathrm{IACD}_{s_0}^{s_0+\xi}(\boldsymbol{x}_0)$ in $\mathcal{V}_\mathrm{L}(t_0)$.

The intersection of a magnetic vortex with a plane can be extracted from a magnetic field by computing the IACD field at the plane, detecting the initial positions of vortex centres as local maxima of IACD, then seeking vortex boundaries as outermost convex closed contours of IACD that encircle vortex centres. In analogy with LAVD, the IACD is an objective and dynamically consistent measure of magnetic element rotation. Specifically, $\mu_0 \times$ IACD gives twice the rotation angle generated by the relative dynamic rotation tensor of equation (2) about its own axis of rotation. The relative rotation tensor is obtained by applying the dynamic polar decomposition (Haller 2016) to the gradient of the flow map generated by the equation (2). The dynamic consistency of IACD then ensures its additivity along magnetic lines, while its objectivity guarantees its invariance under arbitrary, continually varying observer changes along magnetic lines.

The results of applying IACD to the magnetic field of the dynamo simulation at $t_0 = 700$, $z = 0$ and using $\xi = 10$ on equation (3) are shown in Fig. 6. The upper panel shows the contour plot of the IACD field, with two vortex boundaries indicated (again, a convexity deficiency of the order of 10^{-3} is adopted). The same vortices are used as sources of initial conditions for magnetic field lines shown in the other two panels. Note that the integrated field lines are twisted and do not diverge away from each other.

The choice of τ directly impacts the size of the vortices found, both in LAVD and IACD. Larger τ leads to smaller (thinner) vortices, since the layers near a vortex boundary tend to disperse with longer integrations, due to interaction with other vortices and reconnection. We chose $\tau = 10$ because this produces vortices that are not too small in comparison with the energy-injection scale ($2\pi/5$).

4 DISCUSSION AND CONCLUSIONS

The techniques of LCSs can improve our understanding of the dynamics and structures of solar and astrophysical plasmas. Rempel et al. (2011) showed that LCSs are useful for an in-depth analysis of particle transport in dynamo simulations, e.g. the detection of attracting material lines of the velocity field provides the pathways that are more likely to be followed by passive scalars in the plasma; furthermore, the combined detection of attracting and repelling LCSs allows the identification of the main mixing zones of the plasma, which is essential for the study of plasma heating. Chian et al. (2014) studied solar photospheric flows in an active-region plage in the vicinity of AR10930 using the horizontal-velocity data derived from Hinode/Solar Optical Telescope magnetograms and demonstrated the correspondence of the network of high magnetic flux concentrations to the attracting LCSs of the velocity field in the intergranular lanes, comparing the results with numerical simulations of a dynamo driven by turbulent compressible convection with uniform horizontal shear and rotation. Rempel et al. (2013) applied the LCSs method to detect coherent structures straight from the magnetic field of MHD simulations. See also Falessi, Pegoraro & Schep (2015) for a recent work on LCSs and plasma transport processes.

All the aforementioned works deal specifically with hyperbolic LCSs, which are generalizations of stable and unstable manifolds in classic dynamical systems. This Letter presents a work on rotational LCSs in plasmas, where the recent technique of LAVD-based vortex detection is employed to detect vortices in a three-dimensional MHD dynamo simulation. We also adapt the technique to determine the position of magnetic vortices based on the IACD. Both LAVD and IACD provide objective definitions of the vortex boundaries, from where the integrated fluid particles or magnetic field lines display helical pathways with little dispersion. These techniques can aid the study of vortices in solar plasmas, a topic of growing interest from theoretical, numerical and observational points of view. For example, Stenflo (1975) proposed a model for the formation of filament structures of magnetic fields induced by vortical motions around the downdrafts in the solar supergranulation network and active-region plages. Compressive MHD simulations of turbulent convection of solar-type stars performed by Brandenburg et al. (1996) showed that an initially weak magnetic field is amplified and maintained by dynamo action and can be self-organized into magnetic flux tubes that are wrapped around magnetic vortex tubes. Brandt et al. (1988) and Bonet et al. (2008) used the Swedish Solar Telescope at La Palma to detect vortex structures at the downdrafts of the solar atmosphere where the hot buoyant plasma driven by convection returns to the solar interior after cooling down. The pattern of a vortex is derived from the spiral trajectory of magnetic bright points being engulfed by a downdraft (Bonet et al. 2008). Kitiashvili et al. (2012) used radiative MHD simulations to study the formation and dynamics of magnetic vortex tubes generated by turbulent convection, characterized by strong downflows and swirling

motions, which are concentrated mostly in the intergranular lanes of the quiet-Sun. Radiative MHD simulations of magnetoconvection carried out by Shelyag et al. (2011) produced two types of vortices in the photosphere: non-magnetic vortices induced by the baroclinic motions of the phosphoric plasma and magnetic vortices induced by the magnetic tension in the intergranular magnetic flux concentrations. This study indicated that magnetic bright points are subject to rotary motions in the intergranular lanes and are magnetically connected to vortices in the upper photosphere. Wedemeyer et al. (2012) combined ground observations of the Swedish Solar Telescope at La Palma with space observations of *Solar Dynamics Observatory* to identify the swirling motions in the chromosphere as the manifestation of rapidly rotating magnetic structures known as magnetic tornadoes, which reach from the convection zone to the upper solar atmosphere and provide an energy channel from lower to upper solar atmosphere. Their numerical simulations confirmed that the bright points at the photospheric surface are the footprints of magnetic flux concentrations connected to the chromospheric swirls.

In conclusion, the previous demonstration that the technique of hyperbolic LCSs is useful for the analysis of the dynamics of velocity and magnetic fields in numerical simulations (Rempel et al. 2011, 2013) and satellite observations (Chian et al. 2014) of solar plasmas indicates that the novel technique of rotational LCSs can be readily employed to improve the detection of velocity and magnetic vortices in solar and astrophysical turbulence.

ACKNOWLEDGEMENTS

ELR and AC-LC acknowledge Brazilian funding agencies CAPES (Coordination for the Improvement of Higher Education Personnel), CNPq (National Counsel of Technological and Scientific Development) and FAPESP (São Paulo Research Foundation).

REFERENCES

Bonet J. A., Márquez I., Sánchez Almeida J., Cabello I., Domingo V., 2008, ApJ, 687, L131
Brandenburg A., Jennings R. L., Nordlund A., Rieutord M., Stein R. F., Tuominen I., 1996, J. Fluid Mech., 206, 325
Brandt N. P., Scharmer G. B., Ferguson S., Shine R. A., Tarbell T. D., Title A. M., 1988, Nature, 335, 238
Chian A. C.-L., Rempel E. L., Aulanier G., Schmieder B., Shadden S. C., Welsch B. T., Yeates A. R., 2014, ApJ, 786, 51
Chian A. C.-L., Feng H. Q., Hu Q., Loew M. H., Miranda R. A., Muñoz P. R., Sibeck D. G., Wu D. J., 2016, ApJ, 832, 179
Falessi M. V., Pegoraro F., Schep T. J., 2015, J. Plasma Phys., 81, 495810505
Haller G., 2015, Annu. Rev. Fluid Mech., 47, 137
Haller G., 2016, J. Mech. Phys. Solids, 86, 70
Haller G., Hadjighasem A., Farazmand M., Huhn F., 2016, J. Fluid Mech., 795, 136
Kitiashvili I. N., Kosovichev A. G., Mansour N. N., Wray A. A., 2012, ApJ, 751, L21
Lukin V. S., 2014, Plasma Phys. Control. Fusion, 56, 060301
MacTaggart D., Haynes A. L., 2014, MNRAS, 438, 1500
Peacock T., Froyland G., Haller G., 2015, Chaos, 25, 087201
Rempel E. L., Proctor M. R. E., Chian A. C.-L., 2009, MNRAS, 400, 509
Rempel E. L., Chian A. C.-L., Brandenburg A., 2011, ApJ, 735, L9
Rempel E. L., Chian A. C.-L., Brandenburg A., Muñoz P. R., Shadden S. C., 2013, J. Fluid Mech., 729, 309
Shelyag S., Keys P., Mathioudakis M., Keenan F. P., 2011, A&A, 526, A5
Sonsrettee W., Subedi P., Ruffolo D., Matthaeus W. H., Snodin A. P., Wongpan P., Chuychai P., 2015, ApJ, 798, 59
Stenflo J., 1975, Solar Phys., 42, 79
Wedemeyer S., Scullion E., Steiner O., van der Voort L. R., de la Cruz Rodriguez J., Fedun V., Robert Erdélyi R., 2012, Nature, 486, 505

This paper has been typeset from a TEX/LATEX file prepared by the author.